

The Reinforcement Mechanisms of Graphene Oxide in Laser Directed Energy Deposition Fabricated Metal and Ceramic Matrix Composites: A Comparison Study

Yunze Li

Texas Tech University

Dongzhe Zhang

Texas Tech University

Zhipeng Ye

Texas Tech University

Gaihua Ye

Texas Tech University

Rui He

Texas Tech University

Hui Wang

Texas A&M University

Weilong Cong (✉ weilong.cong@ttu.edu)

Texas Tech University <https://orcid.org/0000-0001-6308-7383>

Research Article

Keywords: Graphene oxide, Metal matrix composites, Ceramic matrix composites, Laser directed energy deposition

Posted Date: August 18th, 2021

DOI: <https://doi.org/10.21203/rs.3.rs-790876/v1>

License:  This work is licensed under a Creative Commons Attribution 4.0 International License.

[Read Full License](#)

Version of Record: A version of this preprint was published at The International Journal of Advanced Manufacturing Technology on December 2nd, 2021. See the published version at <https://doi.org/10.1007/s00170-021-08337-z>.

Abstract

Carbon-based nanomaterials mainly including carbon nanotubes (CNTs), graphene, and graphene oxide (GO) have superior properties of low density, outstanding strength, and high hardness. Compared with ceramic reinforcements, a small amount of carbon-based nanomaterials can significantly improve the mechanical properties of metal matrix composites (MMCs) and ceramic matrix composites (CMCs). However, CNTs and graphite always aggregate or degrade during the fabrication with a high temperature, especially in MMCs. GO has the advantages of easier to be dispersed in other materials and better high-temperature stability. Laser directed energy deposition (DED), has been used to fabricate GO-MMCs and GO-CMCs due to the unique capabilities of coating, remanufacturing, and producing functionally graded materials. Laser DED, as a fusion manufacturing process, could fully melt the material powders, which could refine the microstructure and increase the density and mechanical properties. However, GO could react with matrix materials at high temperatures. The survival, degradation, and reactions of GO in laser DED fabricated GO-MMCs and GO-CMCs are still unknown. There is also no investigation on the reinforcement mechanisms of GO in metal matrix materials and ceramic matrix materials in the laser DED process. In this study, GO reinforced Ti (GO-Ti) and GO reinforced zirconia toughened alumina (GO-ZTA) parts were fabricated by laser DED process. Raman spectrum, XRD analysis, and EDS analysis have been applied to investigate the forms of GO in both DED fabricated GO-MMCs and GO-CMCs. The reinforcement mechanisms of GO on microhardness and compressive properties of MMCs and CMCs have been analyzed.

Introduction

Carbon-based nanomaterials, including carbon nanotubes (CNTs), graphene, and graphene oxide (GO), have the advantages of demonstrated low density, high strength, and high hardness, which made them preferable reinforcements to improve the hardness, wear resistance, and compressive properties of metal and ceramic materials [1, 2]. Research works have been carried out to study carbon-based nanomaterials reinforced metal matrix composites (MMCs) and ceramic matrix composites (CMCs) [2–5]. Recently, carbon-based nanomaterials reinforced MMCs and CMCs have been successfully fabricated by different manufacturing processes [6–15]. The results showed that these nanomaterials could improve the hardness, compressive properties, and tensile properties due to their high strength and hardness [4, 5, 16–19]. The self-lubrication properties of carbon-based nanomaterials could also improve the wear resistance of carbon-based nanomaterial reinforced MMCs and CMCs. However, it has been reported that CNTs and graphene are easily decomposed and can react with some matrix materials during the high-temperature fabrication processes [3, 20]. In addition, CNTs and graphene are difficult to be uniformly mixed with metal or ceramic powders [12, 13]. To reduce these disadvantages of CNTs and graphene, GO has been applied to serve as a reinforcement material in metal matrix materials and ceramic matrix materials to improve the mechanical properties. GO has a one-layer carbon atom plate structure with functional groups (such as -OH, =O, -COOH, etc.) that are attached at the edges of GO plates [21]. The functional groups could significantly change the Van der Waals interactions between different plates,

which made GO to be easily dispersed in water and mixed with matrix materials [14]. The functional groups could also increase the stability of GO, which could reduce the possibility to react with matrix materials at a high temperature. In addition, compared with CNTs and graphene, the cost of GO was much lower.

Traditional GO reinforced MMCs and CMCs manufacturing processes had the shortcomings of high energy consumption and shape-restriction [22]. Compared with traditional fabrication processes, laser additive manufacturing (LAM) had the advantages of easy controllability, high stability, and the capabilities of surface modification. Recently, GO reinforced MMCs and CMCs have been fabricated by several LAM processes, including powder bed fusion (PBF) and laser directed energy deposition (DED) [16, 23–25]. Selected laser sintering (SLS), as a kind of PBF process, has been successfully used to fabricate GO reinforced MMCs (such as GO-Ti and GO-Fe) and GO reinforced CMCs (such as GO-Al₂O₃ and GO-ZrO₂) with a relatively low fabrication temperature, which would result in the lower density of the fabricated parts [3, 23, 25, 26]. Compared with the SLS process, the temperature in the SLM and laser DED processes was much higher. The material powers could be fully melted, which contributed to the development of the parts with fine-grained microstructure and high density [27]. Compared with SLM, laser DED had the capabilities of coating, remanufacturing, and producing functionally graded materials. However, it has been reported that GO plates might react with matrix materials during the fabrication due to the high fabrication temperature during the laser DED process [3, 26]. The survival, reaction, and degradation of GO in laser DED fabricated GO reinforced MMCs and CMCs had not been studied. There was also no comparison study on the reinforcement mechanisms of GO on the mechanical properties of laser DED fabricated MMCs and CMCs.

In this study, GO reinforced Ti (GO-Ti) and GO reinforced zirconia toughened alumina (GO-ZTA) parts were fabricated by laser DED process. The survival of GO in Ti and ZTA was analyzed by Raman spectra results, EDS results, XRD results, and microstructure morphology. The different reinforcement mechanisms of GO on the microhardness and compressive properties of MMCs and CMCs were further investigated.

Experiment Procedures

2.1 Materials and powder treatment

GO was in the state of 0.4 wt.% water suspension (Graphenea Inc., MA, USA) with a thickness less than 15 nm. The commercially pure Ti (CP-Ti) powder (99.7% purity) (Atlantic Equipment Engineers Inc., USA) with an average particle size of 50 μm was used in this study. The particle size of Al₂O₃ power (99.9% purity) (Atlantic Equipment Engineers Inc., USA) was 45–75 μm. The particle size of ZrO₂ (99.9% purity) (Atlantic Equipment Engineers Inc., USA) was 1–5 μm.

The powder treatment processes of GO-Ti and GO-ZTA powders were shown in Fig. 2. For the GO-Ti powder, the weight ratio of Ti and GO was 99:1. For the GO-ZTA powder, the weight contents of GO, ZrO₂,

and Al_2O_3 were 1 wt.%, 19.8 wt.%, and 79.2 wt.%. Before the mixing, the GO water dispersion was prepared by the ultrasonic treatment for two hours to suppress the aggregation of GO plates. After that, Ti / Al_2O_3 powder was mixed with GO water dispersion with the assistance of ultrasonic vibration for four hours. Then the mixture was dried by a vacuum Oven (DFA-7000, MTI Corporation, USA) for two days. After that, a planetary ball-milling machine (ND2L, Torrey Hills Technologies LLC., USA) was used to further dry and mix GO-Ti / GO- Al_2O_3 powder. During the ball-milling processes, the sun wheel and the milling jars rotated in opposite directions with a speed of 200 rpm for two hours. The weight ratio between powder and milling balls was 3:1. For GO-ZTA powder, ZrO_2 powder was mixed with prepared GO- Al_2O_3 powder and the mixture was further ball-milled for four hours. After the ball-milling process, GO plates were embedded on the surface of Ti particles. For GO-ZTA powders, GO plates and part of ZrO_2 particles were embedded on the surface of Al_2O_3 particles.

2.2 Experiment set-up

A laser DED system (LENS 450, Optomec Inc., USA) was used to conduct the experiments. To avoid GO plates and Ti reacted with O_2 , the chamber system was purged by argon gas to a low oxygen level (< 50 ppm) before the fabrication. During the fabrication, the powder and gas delivery system delivered the feedstock powders, and the laser system generated and transferred the laser beam to the workpiece at the same time. A molten pool was generated on the surface of the substrate, which caught and melted the materials powders from the delivered powder flow. The molten pool solidified when the laser beam moved away. The deposition head movement was controlled by the control system to fabricate the part following the prepared trajectory. When the first layer was deposited, the deposition head moved up one-layer thickness distance (Z increment), and the second layer was fabricated based on the first layer. By repeating the deposition processes, the parts were deposited layer by layer. The input parameters of GO-Ti and GO-ZTA were listed in Table 1.

Table 1
Laser coating parameters of GO-Ti and GO-ZTA

Input fabrication variables	Value of GO-Ti	Value of GO-ZTA
Laser power (W)	250	275
Beam diameter of laser (μm)	400	400
Wavelength of laser (nm)	1064	1064
Deposit head scanning speed (mm/min)	15	10
Hatch distance (μm)	380	380
Layer thickness (μm)	432	432
Powder feeding rate (g/min)	2.5	2.5
Number of layers	10	10
Oxygen level (ppm)	< 50	< 50
Argon gas flow rate (L/min)	6	6
Scanning orientation ($^{\circ}$)	45, alternate 90 per layer	45, alternate 90 per layer

2.3 Measurement procedures

A scanning electron microscopy equipped with a backscatter electron detector (BSD) was used to observe the microstructure of the powders and the fabricated parts. Before the observation, a grinder-polisher machine (MetaServ 250 single grinder machine, Buehler, USA) was used to grind and polish the cross-sectional surface of the fabricated parts. An energy dispersive X-ray spectroscopy (EDS) system was used to analyze the element compositions of the fabricated parts. To investigate the survival of GO in laser DED fabricated MMCs and CMCs, a Raman spectrometer (HORIBA Jobin Yvon, USA) was used to detect and characterize GO in the fabricated parts, which was one of the most sensitive techniques to characterize GO. A universal tester (AGS-50kNXD, Shimadzu, Japan) was used to test the compressive properties of the fabricated parts with a constant crosshead speed of 0.01 mm/s. Before the compressive testing, the top and bottom surfaces of the fabricated part were ground to parallel. A Vickers hardness tester (Phase II, Upper Saddle River, USA) was used to test the microhardness with the test condition of 9.8 N normal load for 10 s. For each combination of inputs, two samples were used to test the microhardness values. For each sample, the microhardness was tested 10 times on random positions.

Mechanical Properties

3.1 Effects on microhardness

Figure 3 shows the effects of GO on the microhardness of GO-Ti parts and GO-ZTA parts fabricated by the laser DED process. With the addition of GO, the average microhardness values of both GO-Ti parts

and GO-ZTA parts were increased. As shown in Fig. 3(a), there was an overlapping between the error bars of CP-Ti parts and GO-Ti parts. A paired sample t-test was conducted to compare the microhardness. The associated *P*-value (0.019) of these two groups of data was less than 0.05, which indicated that the microhardness value of GO-Ti parts was significantly larger than that of Ti parts. The microhardness of ZTA parts and GO-ZTA parts were shown in the right figure. With the addition of GO, the microhardness value of GO-ZTA parts (1980 HV1.0) was much larger than that of ZTA parts (1680 HV1.0). The additional t-test was not necessary to be conducted. The reasons for the significant increase of microhardness would be further discussed in Sect. 5.1.

3.2 Effects on compressive properties

Figure 4 shows the stress-strain curve and the compressive properties of GO-Ti parts and GO-ZTA parts. As shown in Fig. 4(a1) and Fig. 4(a2), compared with Ti parts, the compressive strength and Young's modulus of GO-Ti parts were higher. However, the addition of GO would slightly decrease the toughness and ductility of GO-Ti parts. The compressive strength, Young's modulus, toughness, and ductility of ZTA parts and GO-ZTA parts were shown in Fig. 4(b2). GO could significantly improve the compressive properties of CMCs. With the addition of GO, the compressive strength and toughness were increased by two times to three times. In addition, Young's modulus and ductility were also significantly increased.

Form Of Go In Mmcs And Cmcs

4.1 Raman spectrum analysis on survival of GO

Figure 5(a) shows the Raman spectrum of air-dried GO before the fabrication. The peaks at around 1360 and 1600 cm^{-1} corresponded to the D peak and G peak of GO, respectively. The D peak was caused by the presence of disorder in sp^2 -hybridized carbon systems in GO. G peak existed from the stretching of the C-C bond in graphitic materials, which was common to all sp^2 carbon systems. Figure 5(b) shows the Raman spectrum of laser DED fabricated GO-Ti parts. Raman peak was not observed in the spectrum from this sample, indicating no GO survived in GO-Ti parts after the fabrication. The possible reason was that most GO decomposed and reacted with Ti during the fabrication [28]. Figure 5(c) shows the Raman spectrum of laser DED fabricated GO-ZTA parts. The emergence of the D peak and G peak in the Raman spectrum of GO-ZTA showed that GO plates survived during the fabrication. It should be noticed that the intensities of D and G peaks were reduced. One of the possible reasons was that during the high-temperature laser DED process, part of GO was decomposed or lost [20]. The second reason was that GO plates were wrapped in liquid state ZTA during the fabrication. After the solidification, the GO plates were distributed in the ZTA matrix and became harder to be detected [25].

4.2 EDS analysis and XRD analysis on element and phase composition

As discussed in Sect. 4.1, Raman spectrum results only proved the decomposition of GO in GO-Ti parts after the laser DED process. The reaction products of GO and Ti were hard to be shown in Raman

spectrum results. Figure 6 shows the composition analysis of GO-Ti parts. EDS analysis was used to investigate the element composition of the fabricated GO-Ti parts. It can be seen in Fig. 6 (a), there were black regions unevenly distributed in light regions. In the EDS results of probe 1, the atomic ratio of Ti to C was around 1:1, which was similar to that of TiC. In addition, the shape and size of the black regions were different from that of GO plates, indicating the occurrence of the reactions. It could be considered that these black regions were TiC particles that were generated during the fabrication. To confirm the phase compositions of these black regions, X-ray power diffraction technology (XRD) was conducted. The XRD patterns of laser DED fabricated Ti and GO-Ti parts were shown in Fig. 6(b). It can be seen that the GO-Ti pattern had the peaks at 2θ degree of 36.5° , 42.4° , and 73.7° , which could be indexed into the phase of TiC. It could be confirmed that most GO reacted with Ti at a high temperature, forming TiC particles. The major element at point 2 was Ti (> 90 at.%), which provided that the light region was Ti matrix. There was also a small composition of C element. The reason was the diffusion of C element during the fabrication. There were ultrafine TiC particles distributed in the Ti matrix [29].

Figure 7 shows the element composition of laser DED fabricated GO-ZTA parts. The element compositions of the black regions (probe 1) were 62.10 at.% carbon, 21.72 at.% oxygen, and 16.18 at.% aluminum. The major element compositions of the GO were carbon (49 at.% – 56 at.%) and oxygen (41 at.% – 50 at.%). It could be found that the element content of the oxygen in the black area was lower than that of the GO that was used in the experiments. The major reason was that the GO was partly decomposed during the fabrication. The functional group that contained oxygen decomposed at high a temperature, releasing CO_2 and H_2O . The reason for the existence of aluminum was that the EDS detected depth ($2\ \mu\text{m}$) was larger than the thickness of the GO plates. The Al_2O_3 matrix under the GO plates was also detected in this measurement. The atom ratio of aluminum to oxygen at grey regions (probe 2) was around 2:3. According to the Al-O phase diagram, there was only one kind of compound between Al and O, which was the Al_2O_3 [30]. It could be confirmed that the grey regions were Al_2O_3 matrix. The element composition of the whit region (probe 3) was 25.43 at.% zirconium, 13.98% aluminum, and 60.59 at.% oxygen. It was reported that the ZrO_2 aggregated at the boundary of Al_2O_3 and generated the network microstructure during the fabrication. Combined with the Al_2O_3 - ZrO_2 phase diagram, the white regions were the mixture of Al_2O_3 and ZrO_2 [31].

Analysis On Reinforcement Mechanisms

5.1 Microstructure characterizations

The microstructure of Ti and GO-Ti parts fabricated by the laser DED process was shown in Fig. 8. It could be observed that some black particles were distributed in light regions. According to the results of Raman spectrum analysis, XRD analysis, and EDS analysis, these black particles were TiC particles that were formed during the fabrication. During the laser DED process, GO plates partly lost the functional groups in the molten pool due to the high temperature [32]. The content of H element and O element was decreased and the content of C element in GO plates became higher. According to the Ti-C phase

diagram. When the temperature of the molten pool came to 1670°C, the liquid Ti could react with C to generate TiC [33]. The reinforcement mechanism of GO in GO-Ti was that TiC particles were formed during the fabrication. Due to the extremely high hardness of TiC, TiC could support the load force and reduce deformation when the indenter of the microhardness tester penetrated in GO-Ti parts during the microhardness tests.

Figure 8 shows the microstructure of ZTA and graphene GO-ZTA parts fabricated by the laser DED process. GO plates were survived in GO-ZTA parts, and there was a clear separation between GO plates and ZTA ceramic matrix. There were two reasons for the survival of GO plates. First, the melting point of GO (about 3600°C) was much higher than that of Al₂O₃ (2072°C) and ZrO₂ (2715°C). During the laser DED process, the ZTA ceramic powders were melted in the molten pool and re-solidified with GO plates, but GO plates were not melted and maintained their original shapes. Second, different from some of the metallic materials, ZTA ceramics could not react with GO even at a high temperature. As discussed in Sect. 3.1, the microhardness of GO-ZTA parts was much higher than ZTA parts. There were two reinforcement effects of GO on GO-ZTA. First, the laser absorbability of GO was lower than Al₂O₃. The addition of GO reduced the temperature of the molten pool and increased the cooling rate during the fabrication, which could refine the grain size of GO-ZTA [27]. With the decrease of the grain size, the microhardness could be increased. The second reason was that GO plates had extremely high hardness and strength. They could support the load and reduce the deformation during the microhardness indentation tests.

5.2 Fracture interface characterizations

Figure 9 shows the features of the fracture interface of GO-Ti parts and GO-ZTA parts. As shown in Fig. 9(a), the fracture marks were relatively evenly distributed in the fracture interface of Ti parts. Some small-sized fracture marks extended to a certain area, forming larger-sized fracture marks. In GO-Ti parts, fracture marks were generated around the formed TiC particles. There were almost no fracture marks in the regions relatively far from TiC particles.

The reason for the higher ultimate compressive strength and Young's modulus of GO-Ti was that the ultrafine stiff particles could transfer the loading from the deformed Ti matrix to themselves during the compressive tests [28]. The TiC particles with higher hardness undertook more loading, which suppressed the dislocation movement and the generation of the fractures inside the Ti matrix (relatively far from TiC particles). Larger stress was required to deform the GO-Ti parts. The lower ductility of GO-Ti parts was caused by the uneven distribution of fractures, resulting in the growth of the fracture to a critical value. The uneven distribution was caused by two major reasons. First, the high-stress concentration occurred in the areas around TiC particles due to the irregular shape of TiC particles. Second, there was a large difference in deformation compatibility between TiC and Ti [34]. Under a similar load, the dislocation movement of TiC and Ti was different, which further intensified the fractures generation in the interfaces of TiC and Ti. GO has little influence on toughness. The toughness was the ability of a material to absorb

energy upon fracture failure, which could be calculated as the area under the strain-stress curve. Although the ultimate compressive strength of GO-Ti parts increased, their ductility was significantly decreased.

Figure 9 shows the features of the fracture interface of laser DED fabricated ZTA parts and GO-ZTA parts. In ZTA parts, the parallel distributed fracture marks had no obvious tendency of disappearance when they went through the grain boundaries. As a comparison, in GO-ZTA parts, fracture marks were significantly suppressed when they extended to the GO plates. In addition, compared with ZTA parts, the number and size of the fracture marks in GO-ZTA parts were significantly decreased.

As discussed in Sect. 4.2.1, GO plates were embedded in the matrix of ZTA. When the fractures extended to GO plates during the compressive tests, GO plates could connect both sides of the fractures to form a bridging condition. It could stop the dislocation movement during the compressive tests, which suppressed the further growth of the fractures. The number and size of fractures were reduced, which contributed to the improvement of compressive properties. In addition, GO plates could undertake the concentrated stress during the compressive tests. It was reported that the graphene-based nanomaterial tended to accumulate around the grain boundaries of ZTA ceramics where the stress was concentrated [13]. Due to the excellent hardness and strength, GO plates increased the energy requirement during the compressive tests. Finally, as discussed in Sect. 4.2.1, GO could refine the grain size of GO-ZTA parts. The smaller grain size could increase the number of high-toughness grain boundaries, which could suppress the dislocations during the compressive tests to enhance the compressive properties [35].

Conclusion

To investigate the effects of GO on the compressive properties, and microhardness of MMCs and CMCs, GO-Ti and GO-ZTA parts were fabricated by the laser DED process in this study. The survival, degradation, and reactions of GO in laser DED fabricated GO-Ti and GO-ZTA parts were analyzed through the Raman spectrum analysis, EDS analysis, and XRD analysis. The microstructure and element distribution of GO-Ti and GO-ZTA composite parts were investigated. The reinforcement mechanism of GO in GO-Ti and GO-ZTA was further studied. The major conclusions are drawn as follows:

1. GO plates reacted with Ti to form TiC particles during the laser DED process. The major reason was that GO lost the oxygen-contained functional groups at a high temperature, promoting the reaction between Ti and C in the molten pool. As a comparison, GO could survive in GO-ZTA parts since it could not react with ZTA at a high temperature.
2. In GO-Ti parts, formed TiC was distributed in the Ti matrix, which had little influence on the microstructure morphology. The microhardness of GO-Ti was improved due to the high hardness of TiC. As a comparison, the microhardness of GO-ZTA was improved by the existence of GO and the refinement of grain size.
3. The ultimate compressive strength and microhardness of GO-Ti were increased due to the high hardness of formed ultrafine TiC particles. The ductility of GO-Ti was decreased due to the uneven

distribution of cracks under the load. Combined with the changes of the ultimate compressive strength and ductility, the toughness of GO-Ti was similar to that of Ti. The compressive properties and the microhardness of GO-ZTA parts were significantly improved. The survived GO could suppress the crack growth, undertaken loads, refine grain size, and uniform the distribution of ZrO₂.

Declarations

Acknowledgments The test of Raman spectroscopy in this study was supported by NSF CAREER Grant No. DMR-1760668.

Funding The test of Raman spectroscopy in this study was supported by NSF CAREER Grant No. DMR-1760668.

Conflict of interest The authors declare no competing interests.

Availability of data and material The data supporting the conclusions are included in the article.

Code availability Not applicable.

Authors' contributions Yunze Li: methodology, investigation, validation, writing—original draft. Dongzhe Zhang: investigation, writing—review and editing. Zhipeng Ye: investigation. Gaihua Ye: investigation. Rui He: writing—review and editing. Hui Wang: writing—review and editing. Weilong Cong: writing—review and editing.

Ethics approval The authors confirm that they have abided by the publication ethics and state that this work is original and has not been used for publication anywhere before.

Consent to participate The authors are willing to participate in journal promotions and updates.

Consent for publication The authors give consent to the journal regarding the publication of this work.

References

- [1] Xu, Z., Shi, X., Zhai, W., Yao, J., Song, S., & Zhang, Q. (2014). Preparation and tribological properties of TiAl matrix composites reinforced by multilayer graphene. *Carbon*, *67*, 168-177.
- [2] Paul, M. C., Sobon, G., Sotor, J., Abramski, K. M., Jagiello, J., Kozinski, R., . . . Pal, M. (2013). A graphene-based mode-locked nano-engineered zirconia–yttria–aluminosilicate glass-based erbium-doped fiber laser. *23*(3), 035110.
- [3] Hu, Y., Wang, H., & Cong, W. (2019). Laser Deposition-Additive Manufacturing of Graphene Oxide Reinforced IN718 Alloys: Effects on Surface Quality, Microstructure, and Mechanical Properties. In *ASME 2019 14th International Manufacturing Science and Engineering Conference*. American Society of Mechanical Engineers Digital Collection.

- [4] Tubio, C. R., Rama, A., Gómez, M., del Río, F., Guitián, F., & Gil, A. (2018). 3D-printed graphene-Al₂O₃ composites with complex mesoscale architecture. *Ceramics International*, 44(5), 5760-5767.
- [5] Yannopoulos, S. N., Siokou, A., Nasikas, N. K., Dracopoulos, V., Ravani, F., & Papatheodorou, G. N. (2012). CO₂-Laser-Induced Growth of Epitaxial Graphene on 6H-SiC (0001). *Advanced Functional Materials*, 22(1), 113-120.
- [6] Fan, Y., Wang, L., Li, J., Li, J., Sun, S., Chen, F., . . . Jiang, W. (2010). Preparation and electrical properties of graphene nanosheet/Al₂O₃ composites. *Carbon*, 48(6), 1743-1749.
- [7] Liu, X., Fan, Y. C., Li, J. L., Wang, L. J., & Jiang, W. (2015). Preparation and mechanical properties of graphene nanosheet reinforced alumina composites. *Advanced Engineering Materials*, 17(1), 28-35.
- [8] Ragulya, A. (2008). Consolidation of ceramic nanopowders. *Advances in Applied Ceramics*, 107(3), 118-134.
- [9] Bonifacio, C. S., Holland, T. B., & van Benthem, K. (2013). Evidence of surface cleaning during electric field assisted sintering. *Scripta Materialia*, 69(11-12), 769-772.
- [10] Luton, M., Jayanth, C., Disko, M., Matras, S., & Vallone, J. (1988). Cryomilling of nano-phase dispersion strengthened aluminum. *MRS Online Proceedings Library Archive*, 132.
- [11] Huang, B., Perez, R., & Lavernia, E. (1998). Grain growth of nanocrystalline Fe–Al alloys produced by cryomilling in liquid argon and nitrogen. *Materials Science Engineering: A*, 255(1-2), 124-132.
- [12] Singh, V., Joung, D., Zhai, L., Das, S., Khondaker, S. I., & Seal, S. (2011). Graphene based materials: past, present and future. *Progress in Materials Science*, 56(8), 1178-1271.
- [13] Yazdani, B., Xia, Y., Ahmad, I., & Zhu, Y. (2015). Graphene and carbon nanotube (GNT)-reinforced alumina nanocomposites. *Journal of the European Ceramic Society*, 35(1), 179-186.
- [14] Compton, O. C., & Nguyen, S. T. (2010). Graphene oxide, highly reduced graphene oxide, and graphene: versatile building blocks for carbon-based materials. *small*, 6(6), 711-723.
- [15] Liu, P., & Zhang, Y. (2011). A theoretical analysis of frictional and defect characteristics of graphene probed by a capped single-walled carbon nanotube. *Carbon*, 49(11), 3687-3697.
- [16] Hu, Z., Tong, G., Lin, D., Nian, Q., Shao, J., Hu, Y., . . . Cheng, G. J. (2016). Laser sintered graphene nickel nanocomposites. *Journal of Materials Processing Technology*, 231, 143-150.
- [17] Hu, Z., Wang, D., Chen, C., Wang, X., Chen, X., & Nian, Q. (2019). Bulk titanium–graphene nanocomposites fabricated by selective laser melting. *Journal of Materials Research*, 34(10), 1744-1753.

- [18] Hu, Z., Chen, F., Xu, J., Ma, Z., Guo, H., Chen, C., . . . Zhang, M. (2018). Fabricating graphene-titanium composites by laser sintering PVA bonding graphene titanium coating: Microstructure and mechanical properties. *Composites Part B: Engineering*, *134*, 133-140.
- [19] Prabhakaran, S., Kumar, H. P., Kalainathan, S., Vasudevan, V. K., Shukla, P., & Lin, D. (2019). Laser shock peening modified surface texturing, microstructure and mechanical properties of graphene dispersion strengthened aluminium nanocomposites. *Surfaces Interfaces* *14*, 127-137.
- [20] Feng, H., Cheng, R., Zhao, X., Duan, X., & Li, J. (2013). A low-temperature method to produce highly reduced graphene oxide. *Nature communications*, *4*(1), 1-8.
- [21] Marcano, D. C., Kosynkin, D. V., Berlin, J. M., Sinitskii, A., Sun, Z., Slesarev, A., . . . Tour, J. M. (2010). Improved synthesis of graphene oxide. *ACS nano*, *4*(8), 4806-4814.
- [22] Huang, L., Geng, L., & Peng, H. (2015). Microstructurally inhomogeneous composites: is a homogeneous reinforcement distribution optimal? *Progress in Materials Science*, *71*, 93-168.
- [23] Hu, Z., Tong, G., Nian, Q., Xu, R., Saei, M., Chen, F., . . . Xu, J. (2016). Laser sintered single layer graphene oxide reinforced titanium matrix nanocomposites. *Composites Part B: Engineering*, *93*, 352-359.
- [24] Boniecki, M., Gołębiewski, P., Wesołowski, W., Woluntarski, M., Piątkowska, A., Romaniec, M., . . . Krzyżak, K. (2017). Alumina/zirconia composites toughened by the addition of graphene flakes. *Ceramics International*, *43*(13), 10066-10070.
- [25] Lin, D., Liu, C. R., & Cheng, G. J. (2014). Single-layer graphene oxide reinforced metal matrix composites by laser sintering: Microstructure and mechanical property enhancement. *Acta Materialia*, *80*, 183-193.
- [26] Huang, X., Yin, R., Qian, L., Zhao, W., Liu, H., Liu, C., . . . Guo, Z. (2019). Processing conditions dependent tunable negative permittivity in reduced graphene oxide-alumina nanocomposites. *Ceramics International*, *45*(14), 17784-17792.
- [27] Farshidianfar, M. H., Khajepour, A., & Gerlich, A. P. (2016). Effect of real-time cooling rate on microstructure in laser additive manufacturing. *Journal of Materials Processing Technology*, *231*, 468-478.
- [28] Zhang, X., Song, F., Wei, Z., Yang, W., & Dai, Z. (2017). Microstructural and mechanical characterization of in-situ TiC/Ti titanium matrix composites fabricated by graphene/Ti sintering reaction. *Materials Science and Engineering: A*, *705*, 153-159.
- [29] Fouilland-Paille, L., Ettaqi, S., Benayoun, S., & Hantzpergue, J. (1997). Structural and mechanical characterization of Ti/TiC cermet coatings synthesized by laser melting. *Surface and Coatings Technology*, *88*(1-3), 204-211.

- [30] Taylor, J., Dinsdale, A., Hilleit, M., & Selleby, M. (1992). A Critical assessment of thermodynamic and phase diagram data for the Al-O system. *Calphad*, 16(2), 173-179.
- [31] Lakiza, S. M., & Lopato, L. M. (1997). Stable and metastable phase relations in the system alumina–zirconia–yttria. *Journal of the American Ceramic Society*, 80(4), 893-902.
- [32] Pei, S., & Cheng, H.-M. (2012). The reduction of graphene oxide. *Carbon*, 50(9), 3210-3228.
- [33] Wu, W. (2010). Dissolution precipitation mechanism of TiC/Ti composite layer produced by laser cladding. *Materials Science and Technology*, 26(3), 367-370.
- [34] Man, H., Zhang, S., Cheng, F., & Yue, T. (2001). Microstructure and formation mechanism of in situ synthesized TiC/Ti surface MMC on Ti-6Al-4V by laser cladding. *Scripta Materialia*, 44(12), 2801.
- [35] Barnett, M., Keshavarz, Z., Beer, A., & Atwell, D. (2004). Influence of grain size on the compressive deformation of wrought Mg–3Al–1Zn. *Acta materialia*, 52(17), 5093-5103.

Figures

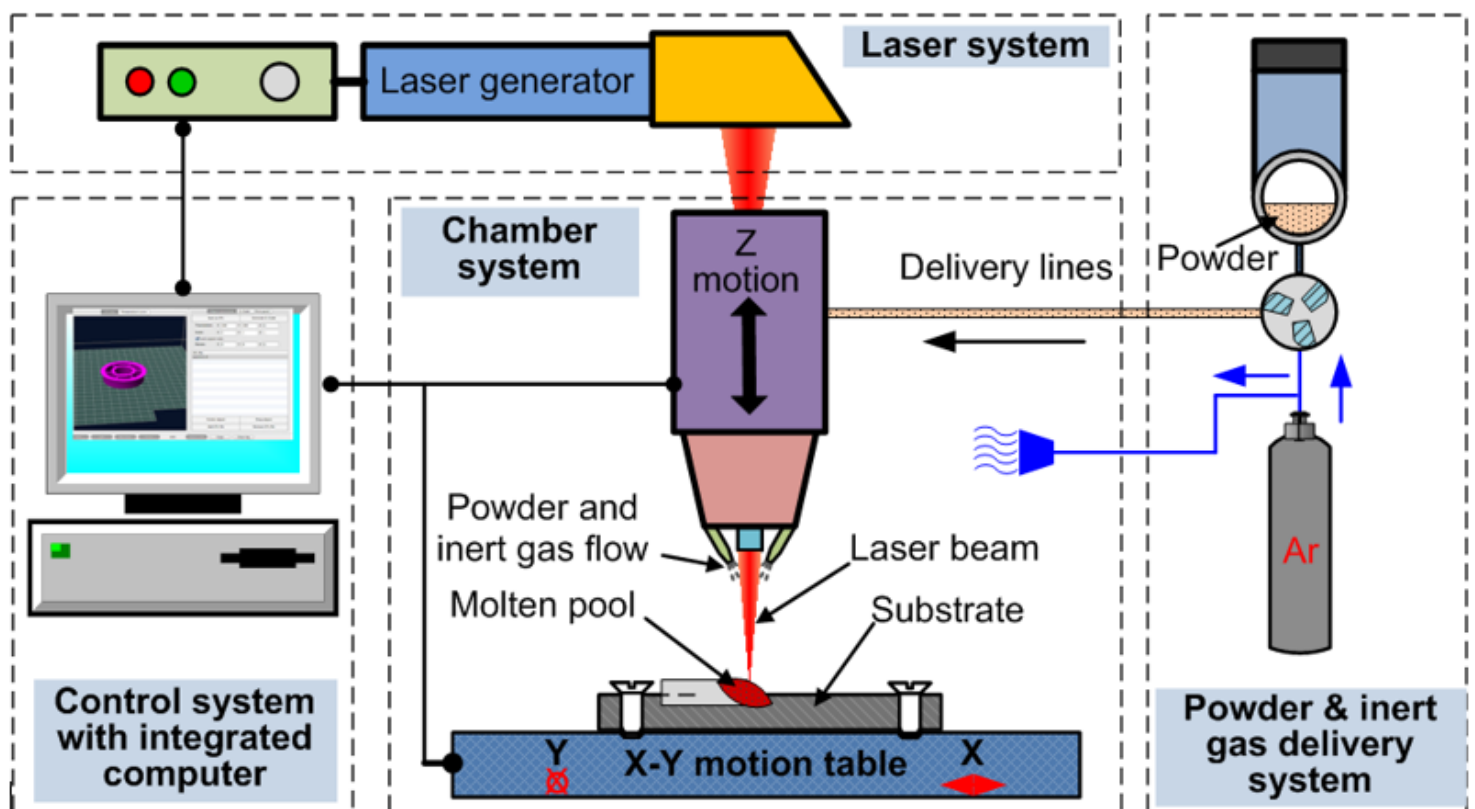


Figure 1

Experimental setup.

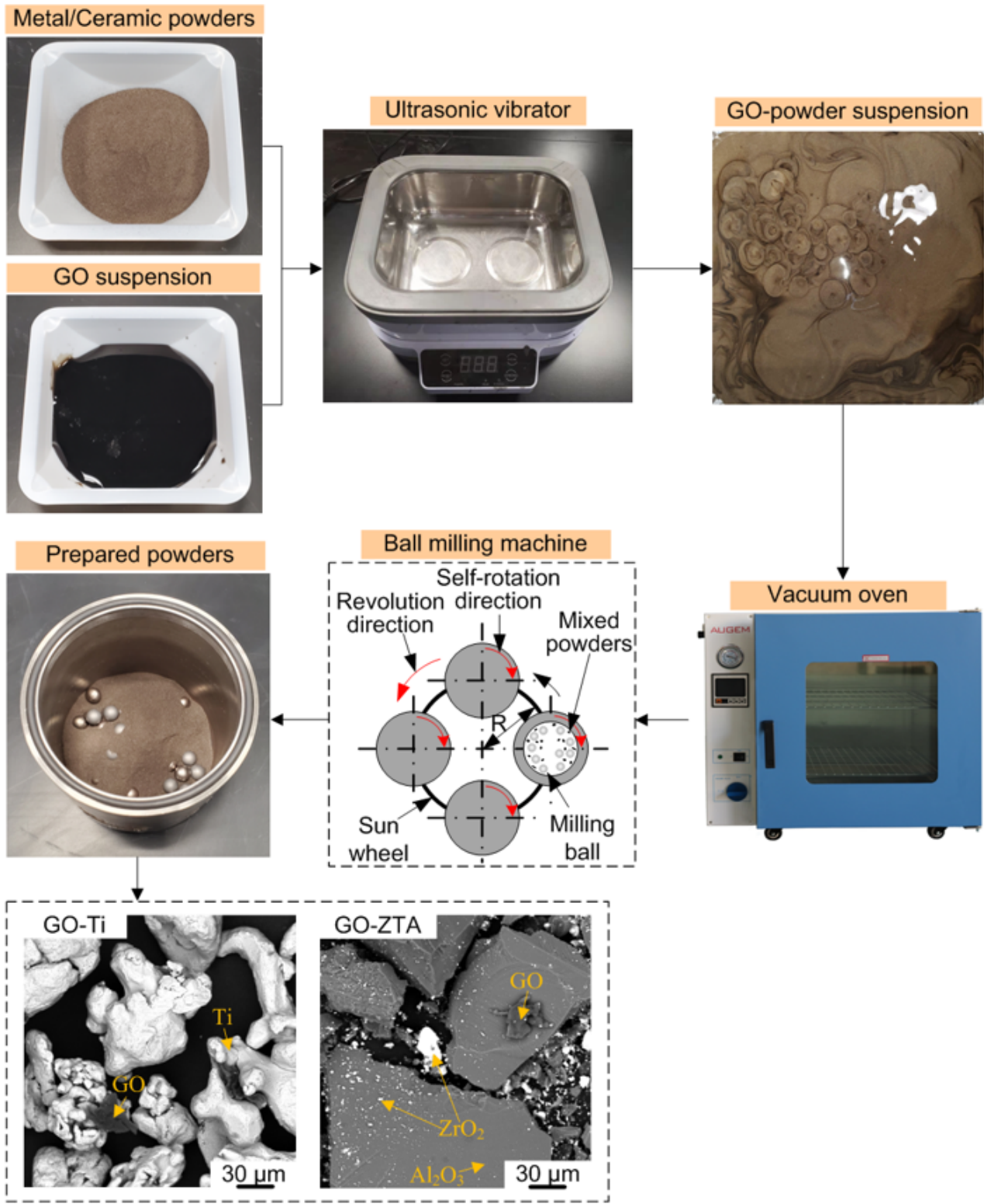


Figure 2

Feedstock powder treatment.

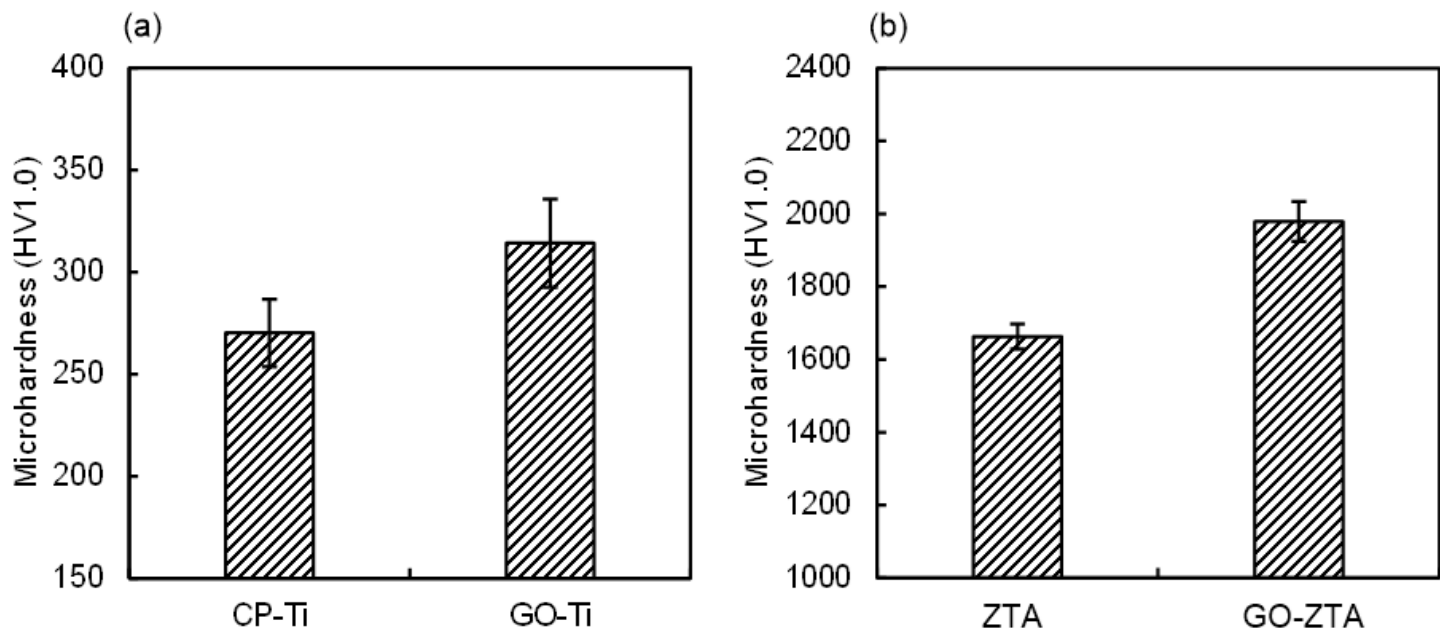


Figure 3

Effects of GO on microhardness of (a) Ti and (b) ZTA parts.

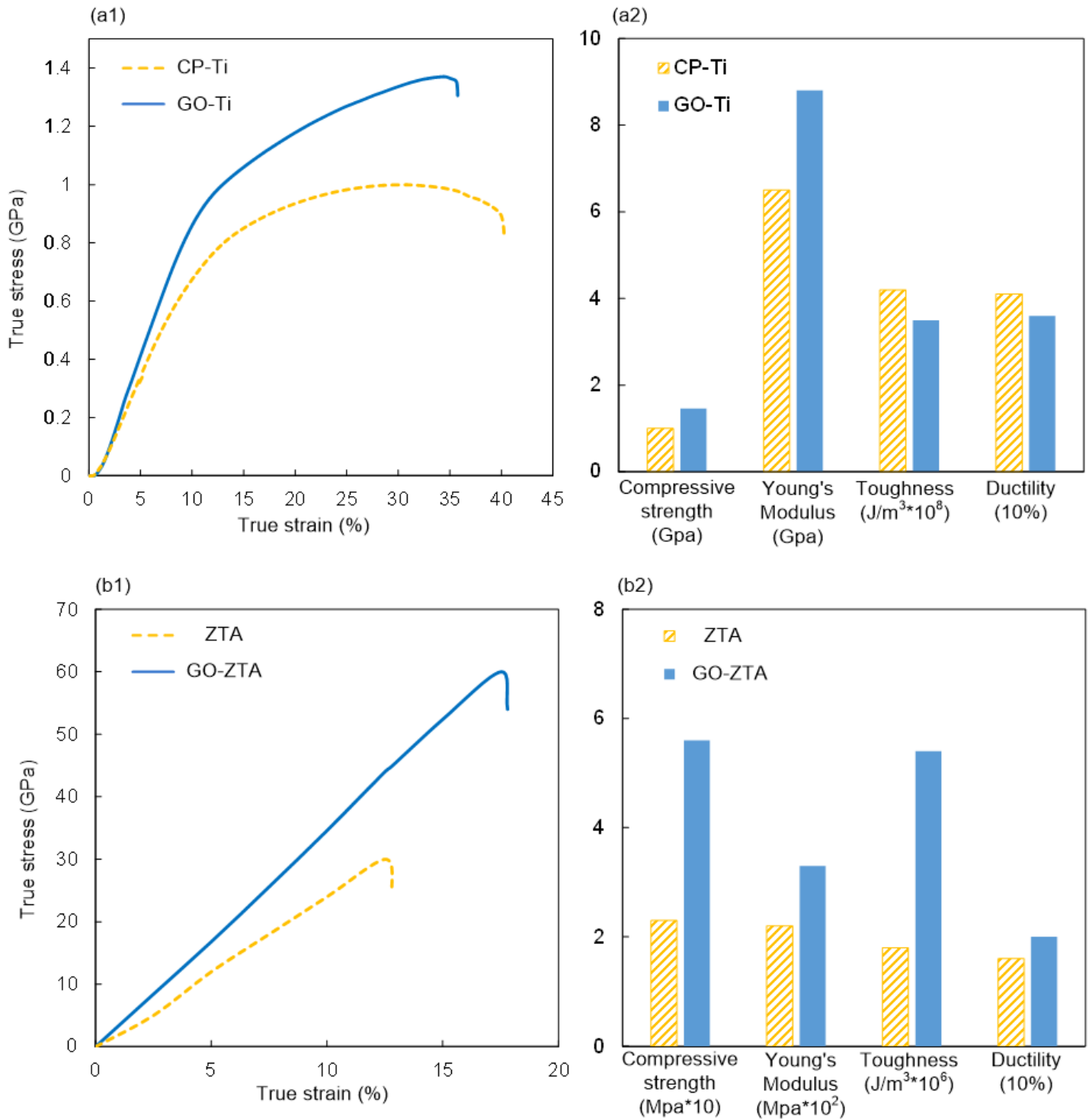


Figure 4

Effects of GO on compressive properties of (a) Ti and (b) ZTA parts.

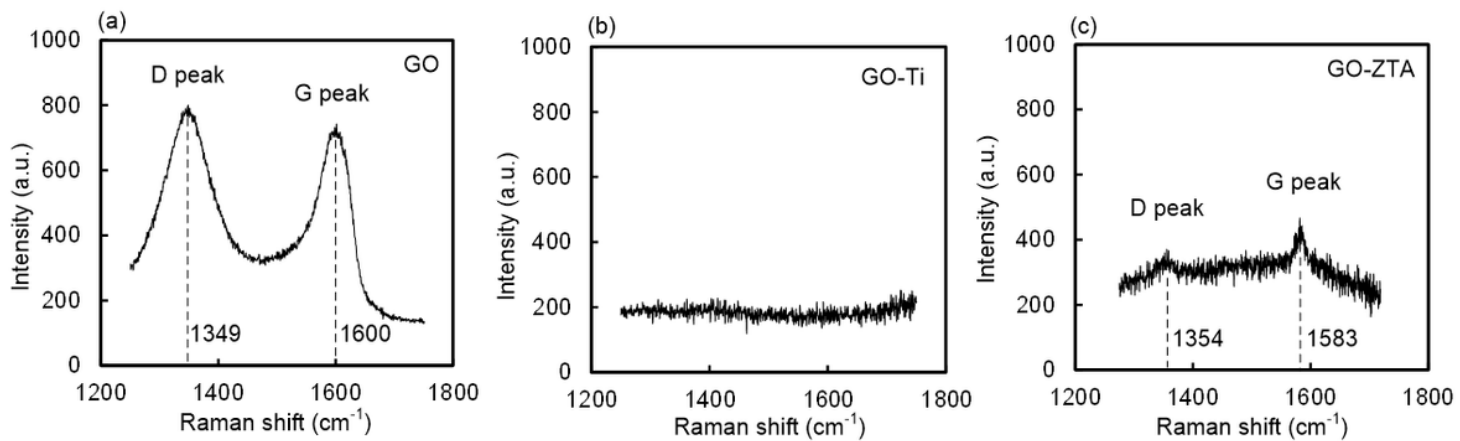


Figure 5

Raman spectra of (a) dried GO, (b) GO-Ti parts, and (c) GO-ZTA parts.

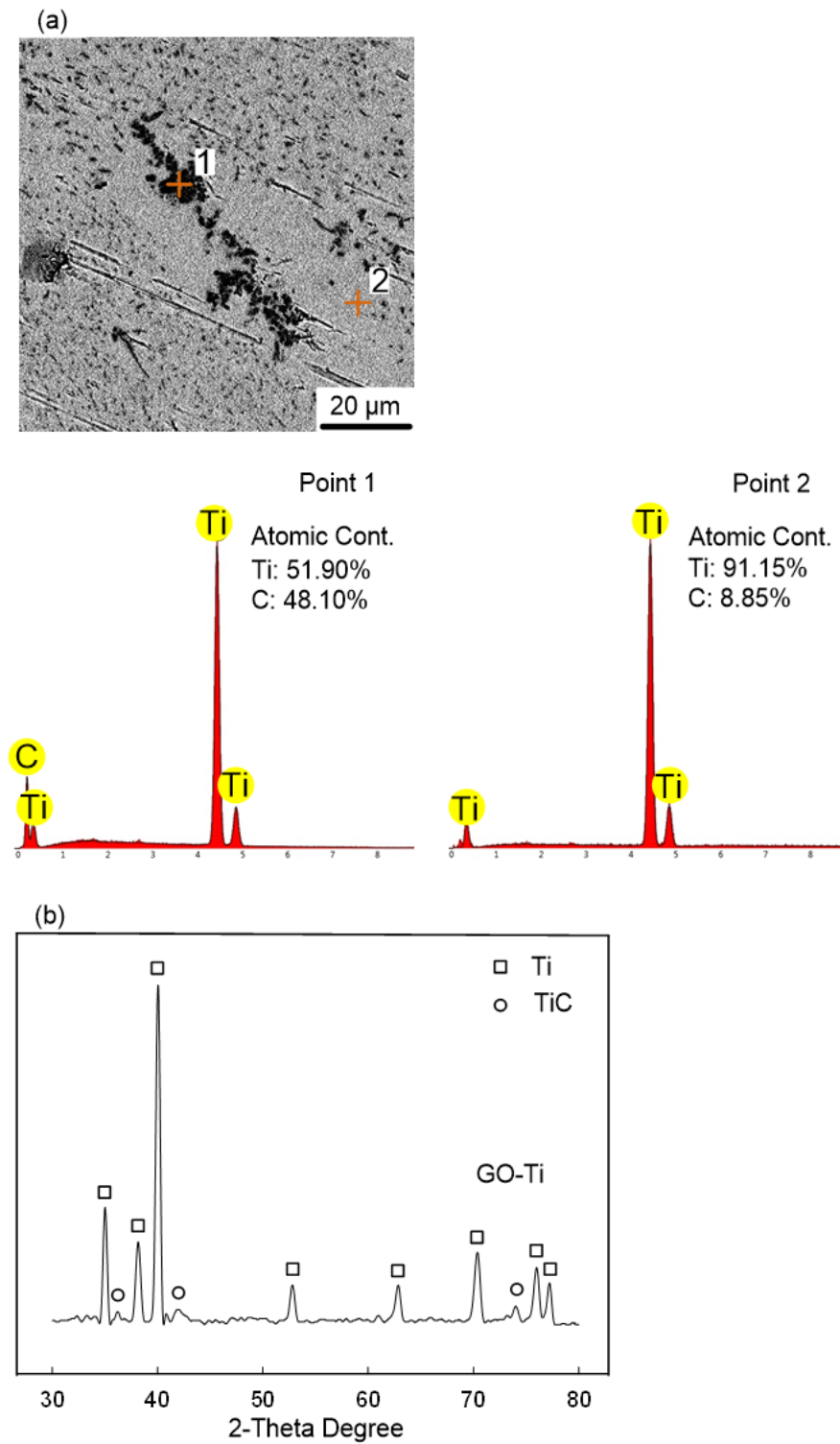


Figure 6

Composition analysis of GO-Ti parts: (a) EDS analysis and (b) XRD analysis.

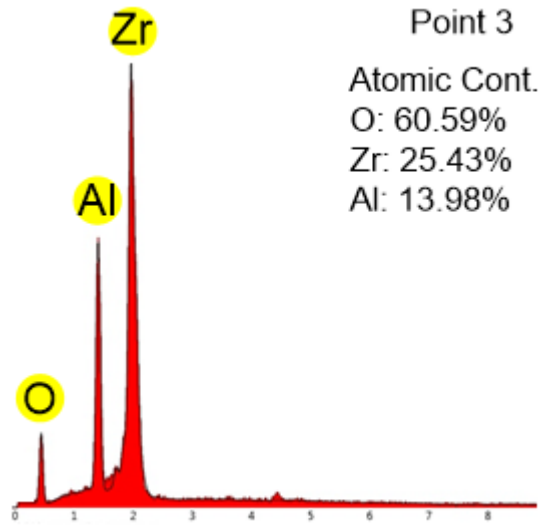
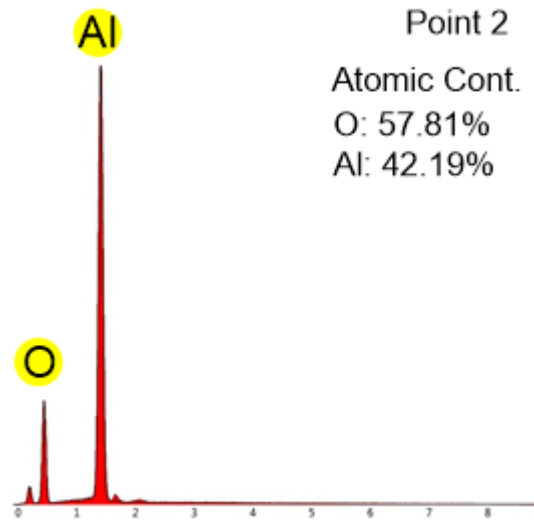
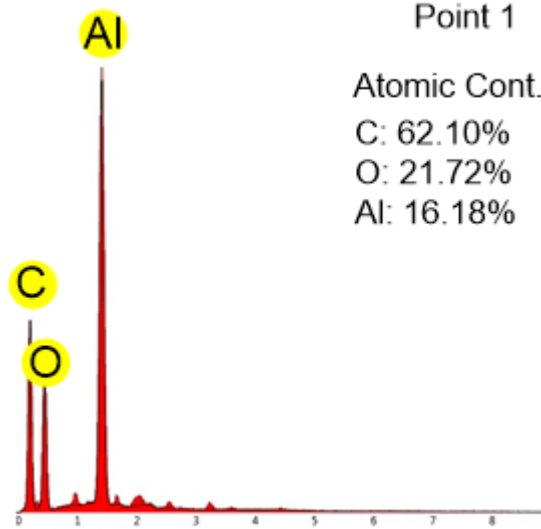
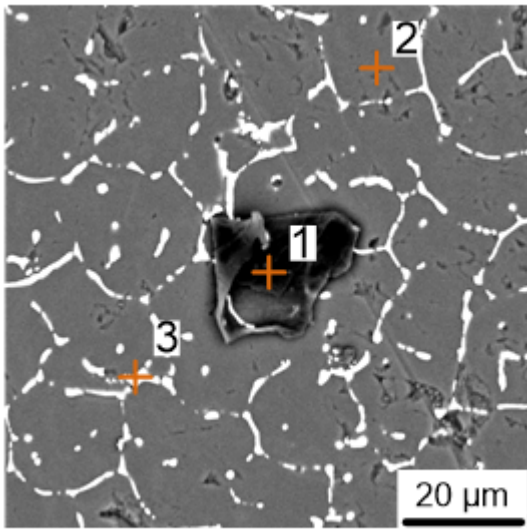


Figure 7

EDS analysis of GO-ZTA parts.

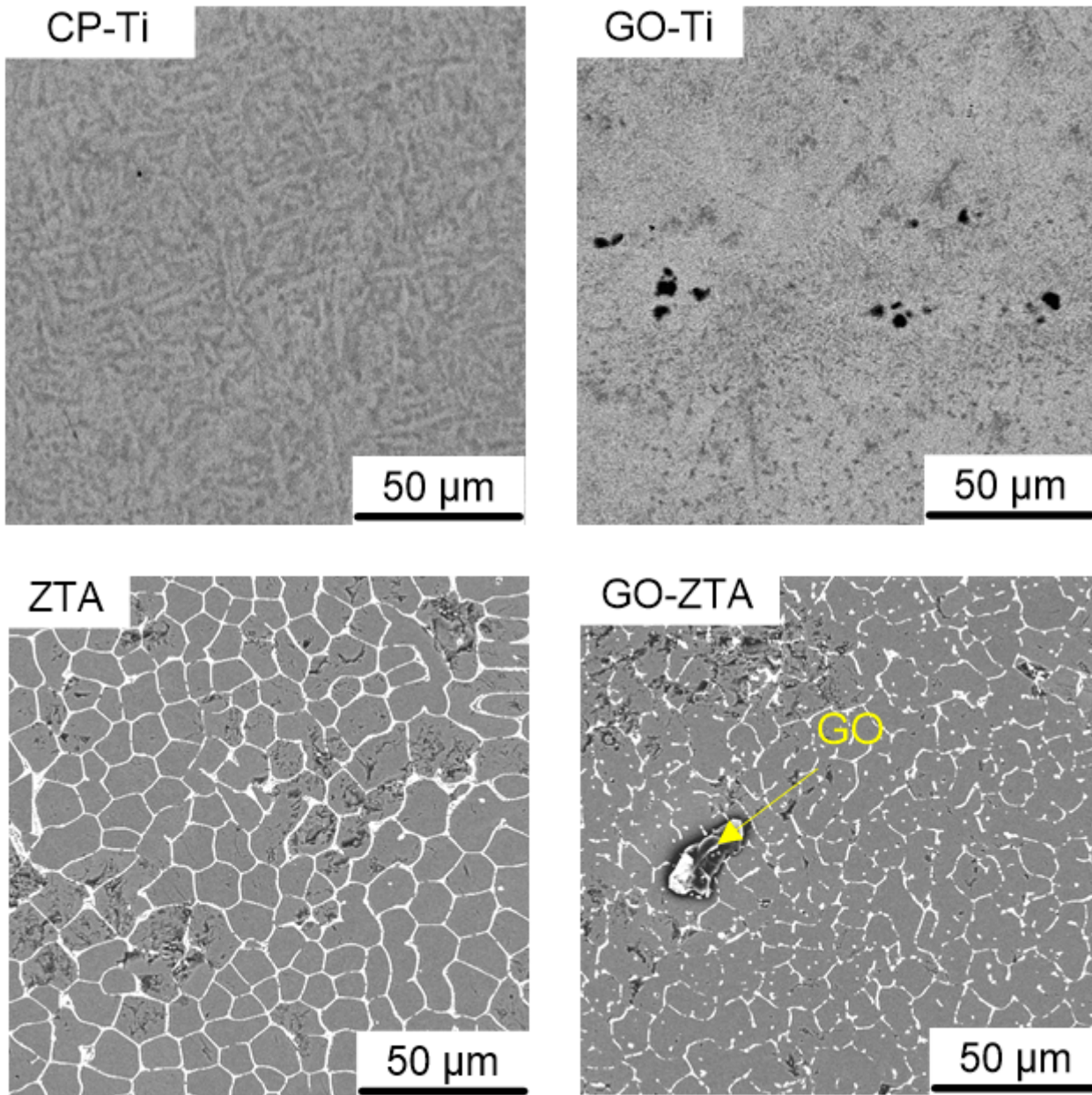


Figure 8

Microstructure of CP-Ti parts, GO-Ti parts, ZTA parts, and GO-ZTA parts.

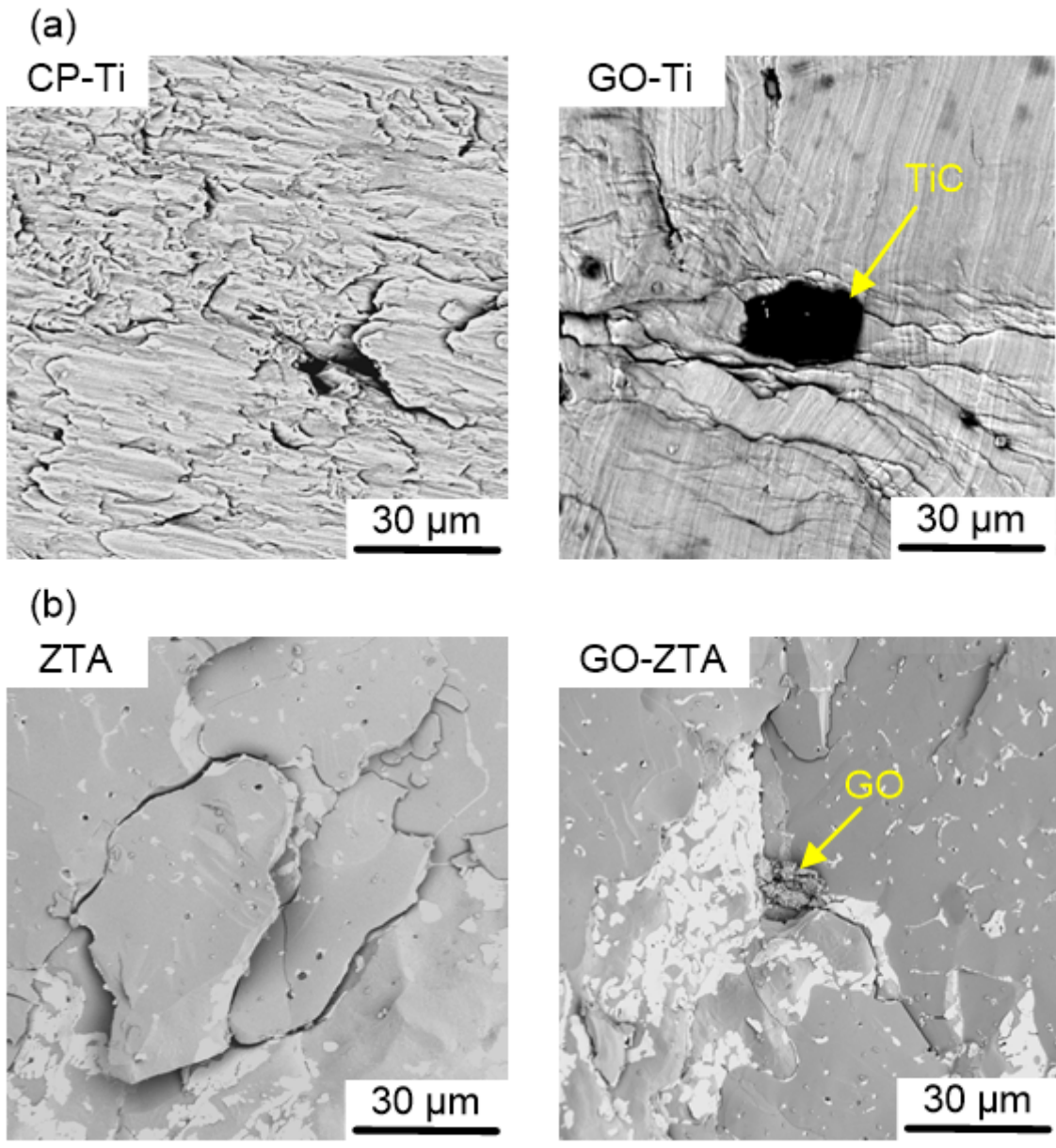


Figure 9

Effects of GO on fracture surfaces of (a) Ti and (b) ZTA parts.